Regular Article - Statistical and Nonlinear Physics

Network configurations of pain: an efficiency characterization of information transmission

Romina De Luise[1], Roman Baravalle[1], Osvaldo A. Rosso[2], and Fernando Montani[1,a]

[1] Instituto de Física de La Plata (IFLP), Universidad Nacional de La Plata, CONICET CCT-La Plata, Diagonal 113 entre 63 y 64, 1900 La Plata, Argentina
[2] Instituto de Física, Universidade Federal de Alagoas (UFAL), BR 104 Norte km 97, 57072-970 Maceió, Brazil

Abstract. Recent studies have shown that gamma-band oscillations are directly related to pain intensity. Pain can be exacerbated or diminished via deactivation or activation of inhibitory interneurons in the dorsal horn. We consider a biologically plausible network model with different proportion of inhibitory neurons to emulate gamma elicited activity during pain processes. We perform an analysis using graph theory to gain further insight in the functional state of the circuitry underlying nociceptive process, considering all the possible gamma elicited configurations of pain when changing the number of inhibitory neurons. The probability distribution of the signal associated with each node or neuron is estimated through the Bandt and Pompe approach. We evaluate the Jensen–Shannon distance between all the possible pairs of nodes/neurons, characterizing the different network configurations by calculating the closeness centrality. Thus, by building the graph properties through the node strength distributions and using an information theoretical approach, we characterize the dynamics of the network configurations of pain. This allows us to identify the nonlinear dynamical structure underlying the nociceptive process. Importantly, our findings show that a network configuration with a 20% of inhibitory neurons boosts information transmission of the complex network circuitry associated with the pain processing.

1 Introduction

A network graph is a schematic representation of a system that depicts the interrelation between objects [1]. Complex networks are connections that depict patterns of links between their components that are neither absolutely random nor simply deterministic. More specifically, a complex network can be characterized by a graph with certain non-trivial statistical and topological properties where the system is composed of many parts; each of them has its own internal structure and is responsible for performing certain functions that affect not linearly the entire network [2]. Our brain is a very efficient complex network, formed by a large number of different brain regions, where each of them has its own task and functions and continually shares information with each other. That is, they form a complex integrated network of inter-connected regions that determine the dynamics and the existing relations between different brain areas.

When talking about brain connectivity, three types of concept must be distinguished that are although related: structural, functional, and effective connectivity [3]. The structural connectivity is referred to the connections between different brain areas, and it is

linked to the anatomical connection properties. That is, they are made by neuronal axons or neuronal tracts that link the different regions, and it is related to the physical environment in which the information transmission is performed [4]. We say that two regions are functionally connected when there is a statistical dependence between the activities of the elements in question, regardless of whether or not they are structurally connected. This type of connectivity is highly dependent on time domain, as opposed to structural, and does not reference to specific directional effects (cause–effect). Thus, that is a statistical concept that depends on the metrics being used, i.e., correlation, covariance, or spectral coherence, etc. [4,5].

When considering effective connectivity, we refer connections that represent causal relationships between different elements. More specifically, when the activation of an area causes a change (activation or depression) in another area, it can be estimated the observed disturbances that describe the directional effects of one neural element on another. Causality can be deduced from disturbances in the network or through analysis of time series. Techniques based on network disturbances often require structural information, while techniques based on time series analysis can be considered "model free" [4]. The weighted links include information about the strength of the connection, and within

[a] e-mail: fmontani@gmail.com (corresponding author)

the framework of functional or effective networks, they can be treated as the magnitude of the correlation or the causality between the nodes [2]. In the study of complex networks, a series of metrics are used to characterize the aspects of connectivity. Node centrality metrics are needed to measure the relative importance of a node within the network architecture. Some centrality metrics have been proposed to quantify the efficiency of a node; among those, we can mention the closeness centrality and the betweenness centrality [4]. The weight of a node is a simple measure for the connectivity of a node with the other nodes in a network. The distribution of weights is defined as the fraction of nodes in the graph that have a given weight. In terms of the shape of the weight distribution, the networks can be classified into different categories that have a different resistance to node removal, for example, in scale-free networks where the node weights are extremely heterogeneous [6].

The central nervous system is the part of the nervous system consisting basically of the brain and spinal cord, and could be considered as a complex network [7–12]. Neuronal centers of the cortical and subcortical areas respond to incoming and ascending pain indicators, which can regulate them through activating the inhibitory descending pathways. The action potential signals descend to the dorsal horn of the spinal wire, and the activated inhibitory interneurons launch neurotransmitters as noradrenaline and serotonine, modulating the pain transmission [8–12]. Endorphins also are in charge within the inhibitory modulation of pain signals. Pain is increased or decreased through the activation or deactivation of inhibitory dorsal horn interneurons [7–12]. Pain-related information inside the central nervous system is managed via variations of inhibitory structures, for instance through the use of endogenous opioids or different endogenous substances like serotonin as inhibitory mediators. Importantly, the dorsal horn gives various potential focuses to the advancement of novel analgesics, and is thought to experience changes that add to the pain aggravation after nerve injury [8–12]. In spite of its conspicuous significance, we lack of knowledge about the neuronal circuits that regulate the inhibitory and excitatory population of neurons in the spinal cord, due to the heterogeneity of the different neuronal segments that make up these circuits [9]. The dorsal horn presents an inhibitory function on the processing of sensory information as a large proportion of inhibitory neurons has been associated with antinociceptive process [9,13]. That is, neurons in the spinal horn process important information, which is then transmitted to a few brain areas, including those accountable of discernment of pain perception. However, there is a huge deficit in understanding which kind of complex network circuitry, with different neuronal inhibitory and excitatory components, may favor the transmission of pain [9,14,15].

The term oscillation or oscillatory activity is referred to rhythmic fluctuations of post-synaptic potentials of a neural ensemble, but also to the rhythmic discharge pattern of action potentials of a neuron or a neuronal group [9,14–16]. Importantly, there is a general consensus that the oscillatory activity constitutes a basic mechanism of the cerebral functioning. Decreases in inhibition lead to changes in frequencies and characteristics of the oscillations, as occurs for example in Parkinson's disease, within the cerebral cortex and other levels. In this way, the appearance or modification of the oscillatory activity can be considered as an indicator of emerging properties of brain [9,14–16]. The central nervous system controls pain information by increasing and decreasing the activity of inhibitory neurons [9,13–15]. When the nociceptive process overcomes, the pain is enhanced or decreased through the deactivation or activation of inhibitory interneurons [7–12]. The gamma-band peaks generated by transient nociceptive boosts are one of the most encouraging biomarkers, as an enhancement of the activity in this band induces pain hypersensitivity [13–15,17–22], and the underlying circuit structure behind the enhancement of the gamma band during nociceptive states is still unknown. In this paper, we investigate the different pain configurations through a biologically plausible neuronal model [23,24]. To it so, we consider different inhibitory and excitatory configurations to capture the effective dynamics of the network when the gamma elicited activity occurs. This allows us to explore the different circuitry structure that may favor the nociceptive process. The main objective of this work is to characterize realistic networks using a simple models capable of capturing the most known firing patterns of neurons, combined with graph theory and information theory tools to identify the different circuitry topologies that present a nociceptive structure related to gamma oscillations patterns. Thus, we take into account different population ensembles with spike-timing-dependent plasticity ($STDP$), in a convolutional spiking neural network, considering different configurations of inhibitory neurons as they have an important nociceptive role on information transmission [7–12]. We combine tools of graph theory and information theoretical measures together with the application of the Bandt and Pompe methodology for time series of membrane potentials, calculating the Jensen–Shannon distance through the different nodes [25]. We calculate the closeness centrality, to identify possible nodes that can mediate communication with others nodes, and evaluating the node strength distributions, we estimate the Shannon entropy, the MPR complexity, and the Fisher information of all the possible nociceptive configurations. This allows us to identify, by estimating Fisher information versus MPR statistical complexity/Shannon entropy of the node strength distributions [13,26–29], the circuitry structure that maximizes information transmission of pain in a biologically plausible neuronal network.

2 Methodology

2.1 Modeling the neuronal system

Neurons fire spikes when they are close to a bifurcation from resting to spiking action, and it is the fragile harmony between chaotic behavior of the recovery variables and the membrane potential, the ion dynamics, and the initial condition what decides the output of the neural action potentials [23,24,30]. While there are an enormous number of conceivable ionic ways of excitability capable of producing an action potential, there are just four bifurcation diagrams that can bring about such progress for a two-dimensional neuron model. That is, there are a lot of ionic ways for producing an action potential, but let us remark that there are just four bifurcations process that can generate them [23,24,30]. These bifurcations separate neurons into four classifications: integrators or resonators, monostable, or bistable [23,24,30].

To understand how the brain works, we need to combine experimental studies of the human and mammals nervous system with numerical simulations on a large scale. As we develop large-scale brain models consisting of firing neurons, we must find a balance between two requirements apparently mutually exclusive: the model for a single neuron must be computationally simple, but capable of producing firing patterns exhibited by biological neurons. The simple model of firing neurons proposed by Izhikevich [23,24,30] is biologically plausible as the Hodgkin–Huxley model [23,24,30], and very efficient from the computational point of view as the Leaky-Integrate-and-Fire Neuron Model [31–33]. Through four parameters, the model successfully reproduces the collective dynamics of the cortical neuronal activity [13,23,24,30]. Bifurcations methodologies allow an accurate reproduction of the biophysical properties of Hodgkin–Huxley neural models using a two-dimensional system of ordinary differential equations of the form: [23,24,30]:

$$\frac{\mathrm{d}v}{\mathrm{d}t} = 0.04v^2 + 5v + 140 - u + I \qquad (1)$$

$$\frac{\mathrm{d}u}{\mathrm{d}t} = a\,(bv - u) \qquad (2)$$

with the auxiliary reset after the action potential:

$$\text{if, } v \geq 30\,\mathrm{mV}, \text{ then } \begin{cases} v \leftarrow c \\ u \leftarrow u + d \end{cases}. \qquad (3)$$

Note that u and v are variables, and a, b, c, and d are four different parameters. The quantity v represents the neuron membrane potential, and u is the membrane recovery variable that takes into account the ionic current of activation of K^+ and of inactivation of Na^+, and generates negative feedback to v. All types of known neuron dynamics can be reproduced by taking different values of the four parameters a, b, c, and d. After the spike reaches its peak at $+30$ mV (not to be confused with the firing threshold), the membrane voltage and the recovery variable are restarted according to Eq. (3). Variable I takes into account the input signals, either injected from the outside or synaptic signals coming from other neurons. The sum $0.04\,v^2 + 5\,v + 140 - u + I$ is obtained by adjusting the initiation dynamics of the spike of a cortical neuron (other choices are possible [13,23,24,30]), whereby the membrane potential v has units of mV and time units of ms. The resting potential in the model is between 70 mV and 60 mV depending on the value of b. As in most real neurons, the threshold is not fixed, which depends on the history of the membrane potential before the spike; it can vary from 55 to 40 mV.

Parameter a describes the time scale of the recovery variable u. Lower values result in slower recovery. A typical value is $a = 0.02$. Parameter b describes the sensitivity of the recovery variable u to subthreshold fluctuations of membrane potential v. Large values of b leads to u and v highly coupled, resulting in possible subthreshold oscillations and decreased threshold. A typical value is $b = 0.2$. The case $b < a$ ($b > a$) corresponds to saddle-node (Andronov–Hopf) bifurcation [30] from the resting state. Parameter c describes the reset value of v after the spike. A typical value is $c = 65$ mV. Parameter d describes the restart, after spike, of recovery variable u and a typical value is $d = 2$. This model can be used to build networks of firing neurons (each neuron can be described by a simple model of firing neuron [23]) capable of exhibiting dynamics and rhythms similar to those of the mammalian cortex. Due to the extreme computational simplicity of the model, thalamic–cortical networks can be simulated consisting of tens of thousands of neurons in real time with a resolution of 1 ms [23,24,30].

In this work, we consider a network model in which the number of inter-connected neurons is a parameter under control, and each neuron can be randomly inter-connected with two or more neurons. Inhibitory contributions hyperpolarize the membrane and move it further from the firing threshold. In contrast, the excitatory contributions depolarize the membrane potential (that is, they carry it closest to the threshold). We emulate a cortical column or hypercolumn that takes into account the firing of cortical neurons with axonal conduction delays and $STDP$ as in Ref. [24]. The time resolution of the network is 1 ms. For the simulation, we consider a network made up of a population of $N = 1000$ neurons, with a number N_e of excitatory neurons (RS), and the number of neurons remaining say N_i will be of inhibitory type (FS), such that $N = N_e + N_i$ [24]. Every excitatory neuron will be randomly connected to $M = 100$ neurons, so that the probability of connection is $M/N = 0.1$ [24]. Each inhibitory neuron will be connected to $M = 100$ excitatory neurons. Excitatory weights evolve according to the $STDP$ rule. Each synaptic connection has a fixed delay D_{sc} between 1 ms and 20 ms. In particular, inhibitory connections have assigned a delay of 1 ms, while for all excitatory connections, the delay will be an integer between 1 and 10 ms. Each neuron in the network is described by the

simple firing neuron model [23]. For all neurons in the network, the values used for the parameters are $b = 0.2$ and $c = 65$. For the excitatory neurons, the parameters are $a = 0.02$ and $d = 8$, corresponding to pyramidal neurons that exhibit regular spiking (RS) patterns. For inhibitory neurons, the parameter are $a = 0.01$ and $d = 2$, corresponding to the cortical interneurons that exhibit fast spiking patterns (FS). The variable I combines two types of inputs to neurons: (1) thalamic random input and (2) firing input from other neurons. Synaptic connections are modified according to the *STDP* rule [24]. We choose the parameters of the *STDP* curve, so that depression is stronger than potentiation and synaptic weight slowly decays to zero. Conversely, if the pre-synaptic neuron often fires earlier than the post-synaptic neuron, then the synaptic connection is slowly boosted. In fact, this connection causes post-synaptic spikes and must be strengthened. In this way, *STDP* strengthens causal interactions in the network. The magnitude of synaptic weights between pre-synaptic neurons depends on the relative time between spikes, in which the temporal order of the pre-synaptic and post-synaptic spikes determines whether a synapse is potentiated or depressed. Every time, a neuron fires the *STDP* variable is reset to 0.1. Every millisecond, *STDP* decreases as $0.95*STDP$, so that it decays to zero as $A \times e^{(-t/\tau)}$. The parameters used here are $\tau = 20$ ms and $A = 0.1$. This function determines the magnitude of the enhancement or depression. For each neuron that fired an spike, we consider all of its pre-synaptic neurons and we determined the times of the last excitatory spikes that arrived from these neurons.

As these spikes caused the neuron to fire, synaptic weights are enhanced according to the *STDP* value in the pre-synaptic neuron adapted for the conduction delay. This corresponds to the positive part of the *STDP* curve [24] where the largest increase occurs for spikes that arrived just before the neuron fire, that is, the spikes that actually caused the post-synaptic spike. Furthermore, when an excitatory spike reaches a post-synaptic neuron, we depress the synapse according to the *STDP* value in the post-synaptic neuron. This corresponds to the negative part of the *STDP* curve [24]. In fact, this spike came after the post-synaptic neuron is fired, and therefore, the synapse between neurons should weaken (the synapse itself will be enhanced when the post-synaptic neuron is activated). Instead of modifying the synaptic weights directly, their derivatives sd are changed as in [24], and then, we update the weights once per second according to the rule $s \leftarrow s + 0.01 + sd$, and $sd \leftarrow 0.9\,sd$, where 0.01 describes the independent increase in synaptic weight activity necessary to enhance synapses that reach silent neurons. Thus, the synaptic change is not instantaneous but slow, and takes many seconds to develop. We manually keep weights in the range between 0 and sm, where sm is a parameter of the model, typically less than 10 mV. This model network preserves important proportions found in the cortex of the mammals. It can also display gamma frequencies in the range of 30–70 Hz, and other interesting rhythms; these kinds of oscillations

are involved in cognitive tasks in humans and other animals.

2.1.1 Bandt and Pompe symbolization methodology

Let $X = \{x_t;\ t = 1, \ldots, M\}$ be a discrete time series, where M is the data number. We consider D and τ_{BP} two integers, such that $D > 1$, $\tau_{BP} \geq 1$, D being the embedding dimension and τ_{BP} the delay time. From the original time series, the following D-dimensional vector could be generated [26,27,34]:

$$X^t_{(D,\tau_{BP})} := \left(x_t, x_{t+\tau_{BP}}, \ldots, x_{t+(D-2)\tau_{BP}}, x_{t+(D-1)\tau_{BP}}\right),$$
$$1 \leq t \leq M - (D-1)\tau_{BP}. \tag{4}$$

Let us consider the *alphabet* $\mathcal{A}_{D \geq 2} := \{\pi_1, \pi_2, \ldots, \pi_{D!}\}$; the set of all possible order permutations D of the set $\mathbf{J} = \{0, 1, \ldots, D-1\}$. We name $\pi_i \in \mathcal{A}_D$ a *symbol of the alphabet* $\mathcal{A}_D$. Let us denote $\pi_i = i_0\ i_1\ \ldots\ i_{D-1}$.

We can assign to $X^t_{(D,\tau_{BP})}$ a symbol $\pi_i \in \mathcal{A}_D$. This assignment must be defined in such a way as to preserve the desired relevant relationship between the elements $x_t \in X^t_{(D,\tau_{BP})}$, and all $t = 1, \ldots, M$ that share this pattern must be uniquely mapped to the same symbol $\pi_i \in \mathcal{A}_D$. In the literature covering Permutation Entropy, there are two ways of defining this mapping of patterns to symbols [26,27,34]:

1. **Permuting the ranges:** sorting the ranges of the $x_i \in X^t_{(D,\tau_{BP})}$ in chronological order: for an arbitrarily given t, the D actual values $x_t \in X^t_{(D,\tau_{BP})}$ are replaced by their ranks, where the rank function is defined as:

$$R\left(x_{t+n}\right) = \sum_{k=0}^{(D-1)\tau} \mathbb{1}\left(x_{t+k} < x_{t+n}\right), \tag{5}$$

where $\mathbb{1}$ is the characteristic function. That is, $\mathbb{1}(Z) = 1$ if Z is true, and 0 otherwise; $x_{t+n}, x_{t+k} \in X^t_{(D,\tau_{BP})}$. In addition, $0 \leq R\left(x_{t+n}\right) \leq (D-1)\,\tau_{BP}$. This means that each $x_t \in X^t_{(D,\tau_{BP})}$ value is replaced by its rank. Thus, the vector $X^t_{(D,\tau_{BP})} = \left(x_t, x_{t+\tau_{BP}}, \ldots, x_{t+(D-2)\tau_{BP}}, x_{t+(D-1)\tau_{BP}}\right)$ is represented by the symbol $\pi_i = \left(R\left(x_t\right), R\left(x_{t+\tau_{BP}}\right), \ldots, R\left(x_{t+(D-1)\tau_{BP}}\right)\right) \in \mathcal{A}_D$.

2. **Permutating the chronological indices:** sorting the i indexes into $x_i \in X^t_{(D,\tau_{BP})}$. Given the vector $X^t_{(D,\tau_{BP})}$, the D values can be ordered in increasing order according to their amplitude, that is:

$$x_{t+i_0\tau_{BP}} \leq x_{t+i_1\tau_{BP}} \leq \cdots$$
$$\leq x_{t+i_{D-2}\tau_{BP}} \leq x_{t+i_{D-1}\tau_{BP}}.$$

Hence, the vector $X^t_{(D,\tau_{BP})} = \left(x_t, x_{t+\tau_{BP}}, \ldots, x_{t+(D-2)\tau_{BP}}, x_{t+(D-1)\tau_{BP}}\right)$ is represented by the

symbol $\pi_i = (i_0, i_1, \ldots, i_{D-2}, i_{D-1}) \in \mathcal{A}_D$.

The relative frequencies for each of the $D!$ possible permutations π_i of order D can be calculated according to the number of times a rearranged sequence corresponding to π_i is founded in the time series, divided by the total number of sequences:

$$p(\pi_i) = \frac{\# \{t \,|\, t \le M - (D-1)\tau_{BP}; \quad t \text{ is of type } \pi_i\}}{M - (D-1)\tau_{BP}}. \tag{6}$$

In this way, the probability distribution is obtained. Here, each symbol π_i representing a pattern in the time series is associated with a probability $P = \{p(\pi_i), \ i = 1, \ldots, D!\}$. For practical reasons, Bandt and Pompe recommended working with $D = 3, \ldots, 6$ and $\tau_{BP} = 1$ [35,36]. To work with reliable statistics, it is needed to accomplish the condition $M \gg D!$.

2.1.2 Permutation entropy

Quantifiers from information theory are a very powerful tool to characterize important properties of the probability density function associated with a time series [13,26–29]. Entropy can be interpreted as a measure of the "degree of disorder", or the uncertainty we have about a system being in a certain state, or of the amount of information that can be obtained through observations of disordered systems [26,27]. When using the Bandt and Pompe probability density function to describe a physical process, the time structure of the signals generated by that process is being taken into account. This allows us to discover important details concerning the ordinal structure of the time series [35,36] and also provides useful feedback about the underlying temporal correlations [37,38].

Below, we introduce the concept of entropy [39], which is a measure of uncertainty/lack of information of a random variable [39,40]. Consider a discrete random variable X, the state space $\mathcal{X}$ of X, that is, the set of possible outcomes, and the probability density function $p(x) = P(X = x)$ of X. The *entropy* $S[X]$ of a discrete random variable X is defined by:

$$S[X] = -\sum_{x \in \mathcal{X}} p(x) \log(p(x)). \tag{7}$$

Entropy is a measure of the average uncertainty in the random variable. Note that entropy is a function of the distribution of X and does not depend on the values that the variable X takes, but instead on the probabilities.

The *relative entropy* or *Kullback–Leibler divergence* between two probability functions $p(x)$ and $q(x)$ is defined by:

$$D_{KL}(p\|q) = \sum_{x \in \mathcal{X}} p(x) \log \frac{p(x)}{q(x)}. \tag{8}$$

Relative entropy is always non-negative and is zero if and only if $p = q$. For this property, it is often used the Kullback–Leibler divergence as a measure of dissimilarity between probability distributions. However, it is not an actual distance between distributions, since it is not symmetric and does not satisfy the triangular inequality.

2.2 Jensen–Shannon divergence

The Kullback–Leibler divergence is not symmetrical, does not qualify as a statistical metric, and does not has an upper bound. Because of these limitations, let us introduce the so-called Jensen–Shannon divergence:

The *Jensen–Shannon divergence* between two probability density functions $p(x)$ and $q(x)$ is defined as:

$$D_{\mathrm{JS}}(p\|q) = \frac{1}{2}\left(D_{KL}\left(p \left\| \frac{p+q}{2}\right.\right) + D_{KL}\left(q \left\| \frac{p+q}{2}\right.\right) \right). \tag{9}$$

We can rewrite the Jensen–Shannon divergence as:

$$D_{\mathrm{JS}}(p\|q) = -\frac{1}{2}\left(S[p] + S[q]\right) + S\left[\frac{p+q}{2}\right]. \tag{10}$$

The Jensen–Shannon divergence is symmetric, non-negative, and is equal to zero if and only if $p = q$ and the square root of the Jensen–Shannon satisfies the triangular inequality. These properties make D_{JS} a metric and a good measure of dissimilarity between two probability distributions.

2.3 Fisher information

Fisher's measure of information can be interpreted as a measure of the quality of a parameter estimation process, such as the amount of information which can be taken from a set of measures, or as a measure of the disorder of a system or phenomenon: [41].

$$F[f] = \int \frac{|\overrightarrow{\nabla} f(x)|^2}{f(x)}\, \mathrm{d}x, \tag{11}$$

where f is a continuous density function, and $\overrightarrow{\nabla}$ is the gradient operator. The presence of the gradient implies a sensitivity of this quantifier to small perturbations of the probability density function, so this quantifier is called "local".

It would be convenient if $f(x)$ did not appear in the denominator in Eq. (11), since it could happen that $f(x) \to 0$ for certain values of x. One way to avoid this possible drawback is to work with an "amplitude" function ψ, $f(x) = \psi^2(x)$. From this and from Eq. (11), we obtain that:

$$F[f] = F[\psi] = 4 \int |\overrightarrow{\nabla}\psi|^2\, \mathrm{d}x, \tag{12}$$

is an equivalent form where it is clearly seen that Fisher's information measure is a measure of the gradient content of $\psi(x)$ and therefore of $f(x)$.

Let us consider the probability function $P = \{p_i, i = 1, \ldots, N\}$, corresponding to a discrete random variable X, where N is the number of possible states of the system under study. In the current work, we use the normalized discrete Fisher information [29], which is given by:

$$F[P] = F_0 \sum_{i=1}^{N-1} \left[\sqrt{p_{i+1}} - \sqrt{p_i} \right]^2, \tag{13}$$

where F_0 is a normalization constant:

$$F_0 = \begin{cases} 1 & \text{if } p_{i*} = 1 \text{ for } i* = 1 \text{ or } i* = N \text{ and } p_i \neq 0 \; \forall i \neq i*, \\ \frac{1}{2} & \text{opposite case} \end{cases}. \tag{14}$$

2.4 Statistical complexity

The notion of zero "complexity" in physics begins with the perfect crystal and the isolated ideal gas as examples of very simple models. In a perfect crystal, the atoms are organized in a symmetrical way, the probability density is concentrated in a single state, that is, there is a most likely state x_c that has $p(x_c) \sim 1$, and for all the other states $x_i \neq x_c$, the probabilities accomplishes $p(x_c) \sim 0$. The "information" stored in this system may be considered minimal. On the other hand, if we consider the isolated ideal gas that is completely disordered, the system can be founded in any of its x_i accessible states with the same probability; that is, $p(x_i) \sim \frac{1}{N}$. Thus, the "information" needed to describe the system is maximum. These two simple systems are located at opposite ends of "order" and "information". It follows that the definition of "complexity" should not be made uniquely in terms of "order" or "information".

Suppose that we have a system with N states, $(x_1, x_2, \ldots, x_N)$ with their corresponding probabilities $P = \{p_1, p_2, \ldots, p_N\}$ $\left(\text{such that } \sum_{i=1}^{N} p_i = 1 \right)$. A possible definition of *disequilibrium E* of the system could be associated with some type of distance between the distribution of the system and the distribution of the equiprobable states, for example, when we take the Euclidean distance:

$$E[P] = \sum_{i=1}^{N} \left(p_i - \frac{1}{N} \right)^2. \tag{15}$$

The Euclidean-like measure of *statistical complexity* C associated with the physical process described by P is defined as an interaction between a distance of the system distribution to the equiprobable distribution (or equilibrium), and the entropy [42], as follows:

$$C[P] = S[P] \cdot E[P] \tag{16}$$

$$= \left(-\sum_{i=1}^{N} p_i \log p_i \right) \left(\sum_{i=1}^{N} \left(p_i - \frac{1}{N} \right)^2 \right). \tag{17}$$

This definition conforms to intuitive reasoning. For a crystal, E is great, but the information S is very small, so $C \sim 0$. On the other hand, S it is large for an ideal gas, but E is small, so $C \sim 0$. Any other system will have a behavior in between and therefore $C > 0$.

For the above described complexity, $C = S \cdot E$, one can get a family of measures of statistical complexity using the different standard entropies. That is, we could use for instance the Shannon [39], Tsallis [43], or Rényi [44] entropy measures. In addition, the disequilibrium can be assessed with measures of distances that could be based for instance on the Euclidean standard idea [42], the Wootters' distance [45], the Kullback–Leibler divergence [46], or the Jensen–Shannon divergence [47–50]. However, the definition above using the Euclidean distance has been widely criticized [45]. The main problem is that it ignores the fact that we are dealing with a probability space, and therefore, it bypasses the stochastic nature of the P distribution [45]. To account for the stochastically nature of the data, we choose in this paper a disequilibrium measure based on Jensen–Shannon divergence [47–50]. The complexity that uses Jensen–Shannon's distance is known as MPR complexity, since it was introduced by Martín, Plastino, and Rosso [49,50]. Let us say that P is the distribution of the system to be analyzed, P_e is the equilibrium probability distribution, N is the number of possible states, $H = S[P] / \log(N)$ is the normalized Shannon entropy, D_{JS} is the Jensen–Shannon divergence [47–50], and Q_0 is a normalizing constant equal to the inverse of the maximum possible value of $D_{JS}(P \| P_e)$ which is obtained when one of the components of P, say p_j, is equal to one and the remaining components are zero. The MPR complexity is given by:

$$C_{MPR}[P] = Q_0 \cdot D_{JS}(P \| P_e) \cdot H[P], \tag{18}$$

where:

$$Q_0 = -2 \left(\frac{N+1}{(N+1) - \log(2N) + \log(N)} \right)^{-1}. \tag{19}$$

Note that the MPR complexity is also a normalized quantifier $0 \leq C_{MPR}[P] \leq 1$. We introduce in the following paragraph some measures of centrality to quantify the structure of a network. If we know the structure of a network, we can calculate from it a variety of useful quantities or measurements that capture particular characteristics of the network topology [25,51–56].

2.5 Centrality measures

Let us consider a weighted graph (G, w) with N nodes, the *shortest path*, or *geodesic path* between two nodes n_i and n_j, is a path for which the sum of the edge weights

is minimal. The *geodesic distance* between two nodes n_i and n_j, noted by $d^w(n_i, n_j)$, is the sum of the weights of the edges of a geodesic path between the nodes n_i and n_j.

Given a weighted graph (G, w) with N nodes, the *closeness centrality* of a node n_i is given by:

$$C_c^w(n_i) = \frac{N-1}{\sum_{\substack{j=1 \\ n_j \neq n_i}}^{N} d^w(n_i, n_j)}.$$

The closeness centrality provides higher values for more central nodes and lower values for less central nodes. This quantity takes higher values for nodes that are separated from others by a short geodesic distance. Such nodes could have a better access to information or a more direct influence on other nodes. In a social network, for example, a person with a high degree of closeness centrality may find that their opinions reach other people in the community more quickly than the opinions of someone with a lower level of closeness centrality [25,51–56].

Given a weighted graph (G, w), with $n_i, n_j, n_k \in V(G)$ (with $V(G)$ being the ensemble of all the node graphs), $i, j, k = 1, \ldots, N$. The *betweenness centrality* of the node n_k is given by:

$$C_b^w(n_k) = \sum_{\substack{n_i, n_j \in V(G) \\ n_i, n_j \neq n_k}} \frac{g_{ij}(n_k)}{g_{ij}},$$

where $g_{ij}(n_k)$ is the number of geodesics between n_i and n_j that pass through n_k, and g_{ij} is the number of geodesics between n_i and n_j.

Betweenness centrality quantifies the occasions a node lies on the shortest path between other nodes. This measure shows which node are bridges between nodes in a system. It does this by identifying all the shortest paths and then counting how many times each node falls on them [51–56].

3 Results

It has been documented that neural oscillations are able to cover a wide spectrum of frequencies. These oscillations are observed at all levels of the central nervous system and are generally classified into five frequency bands: delta 0.5–3.5 Hz, theta 4–7 Hz, alpha 8–12 Hz, beta 13–30 Hz, and gamma > 30 Hz [16]. Gamma band is the essential feature for understanding information processing in pain perception and the structures underlying the neural circuits behind the activity patterns [13–15,17–19,21,22].

In this section, we study the degree of network inter-connectivity, and how closeness centrality and betweenness centrality vary by changing the number of inhibitory neurons in the network for "pain" configurations; that is, those configurations for which the

network exhibits gamma oscillations. The modeled network consists of a population of $N = 1000$ neurons, with N_e excitatory and N_i inhibitory neurons, so that $N = N_e + N_i$. Each excitatory neuron will be connected randomly with $M = 100$ neurons. Excitatory weights evolve according to the *STDP* rule [24]. Using the Bandt and Pompe approach to generate probability distribution [26,27,34], which take into account the causality of the signal, and based on the degree of network inter-connectivity, we build in this section the information quantifiers normalized Shannon Entropy vs. MPR Statistical Complexity [26,27], $H \times C_{MPR}$, normalized Shannon Entropy vs. Fisher information $H \times F$ [26,27], and MPR Statistical Complexity vs. Fisher information $C_{MPR} \times F$ [26,27].

To select the gamma settings in neuronal network, we display the spiking activity of the population through the figure so-called raster plot, as shown in Fig. 1, where each point represents an action potential and each row represents the activity of a neuron in a 1 s window. The y-axis corresponds to the neuron index, and the x-axis corresponds to the simulation time. The presence of a point with coordinates (t, i) indicates that the $i-th$ neuron produced an action potential at time t. Figure 1 depicts an example of a particular pattern of activity, "recorded" during 1 s, for a simulations carried out with $N = 1000$ neurons, with $N_e = 798$ and $N_i = 202$. Figure 1 depicts a quite remarkable oscillatory activity.

To explore better the information underlying neuronal dynamics during the oscillation process, we estimated the histogram of the number of action potentials in the network in each ms and we performed an analysis of the power spectrum using Fast Fourier Transform (FFT) [57]. The FFT breaks down the signal in a series of sinusoidal components [57]. The square of the coefficients is named power. The spectrogram of the population spikes reveals the presence of oscillations. We set the simulation to stop when there are gamma rhythms, i.e., when there is peak in the 30–70 Hz frequency range.
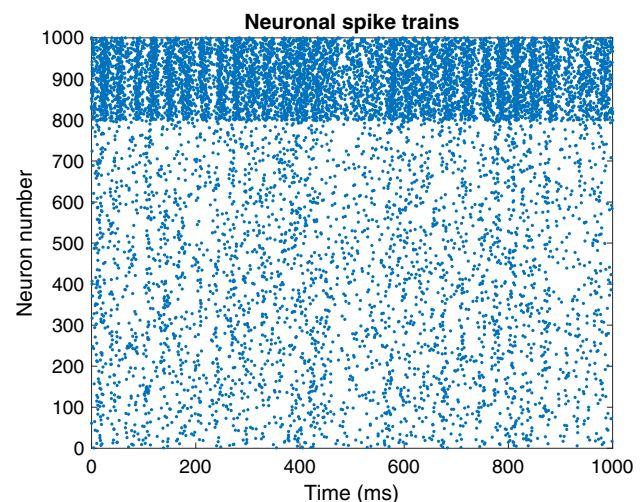
Fig. 1 Raster plot. As synaptic weights evolve following the *STDP* rule, the gamma oscillations dominate
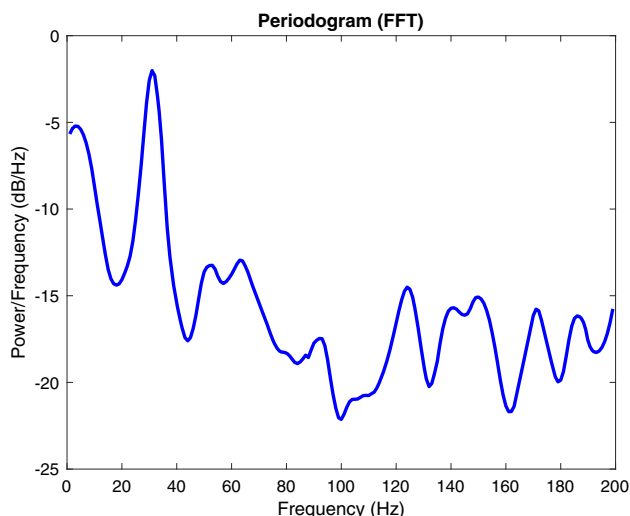
Fig. 2 Power spectrum of the number of action potentials in each spike trains of 1 ms. A peak is observed around 31 Hz (gamma rhythmic)
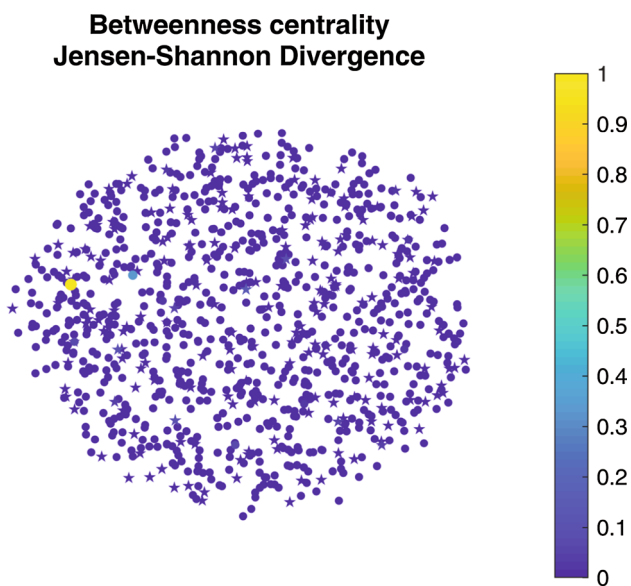

Fig. 3 The weighted network nodes and their closeness centrality (normalized values). The weighted network are constructed using the Jensen–Shannon divergence. The total number of neurons is $N = 1000$; $N_i = 202$ represents the inhibitory neurons (pentagrams); $N_e = 798$ represents the excitatory neurons (circles)

That is, we only select the configurations that present gamma oscillations. Figure 2 shows the gamma band elicited peak due transient nociceptive circuitry dynamics considering a population of neurons with $N_e = 798$ and $N_i = 202$ and taking 1000 ms of sustained activity.

To apply the centrality measures described above, for each of the neuronal configurations that present gamma rhythmic elicited activity, we will now explain the procedure used to construct the weighted graphs. Each neuron in the network is represented by a node, so in each network, the total number of nodes is 1000. To assign weights and connections between the nodes, we will first select the membrane potential v of each of the neurons. These membrane potentials are the time series to which we will apply the symbolization proposed by Bandt and Pompe [26,27,34], using the mapping of patterns to symbols according to the chronological order, dimension $D = 5$, and delay time $\tau_{BP} = 1$, as the time series length is $1000 \gg 5!$. That is, we have 1000 points in the time series $X_i = \{x_t; t = 1, \ldots, 1000\}$, associated with $5! = 120$ possible patterns. For each pair of these density functions $P_i(x)$ and $P_j(x)$, we calculate the Jensen–Shannon divergence: $D^{ij} := D_{\text{JS}}(P_i \| P_j)$, $i, j = 1, \ldots, N$, $i \neq j$, which assigns the inter-connectivity (weight) between neuron i and neuron j. We construct weighted graphs where the set of vertices represents the neurons and each pair of vertices is connected by an edge whose weight is given by $w_{ij} = D^{ij}$.

Figure 3 shows the weighted network nodes and their closeness centrality, while Fig. 4 shows the weighted network nodes with their betweenness centrality.

The weighted network in both figures is constructed using the divergence from Jensen–Shannon with $N = 1000$ neurons, $N_i = 202$ are inhibitory neurons, and $N_e = 798$ excitatory neurons. In Figs. 3 and 4, the shape of the nodes indicates whether it represent excitatory (circle) or inhibitory (pentagram) neurons. In
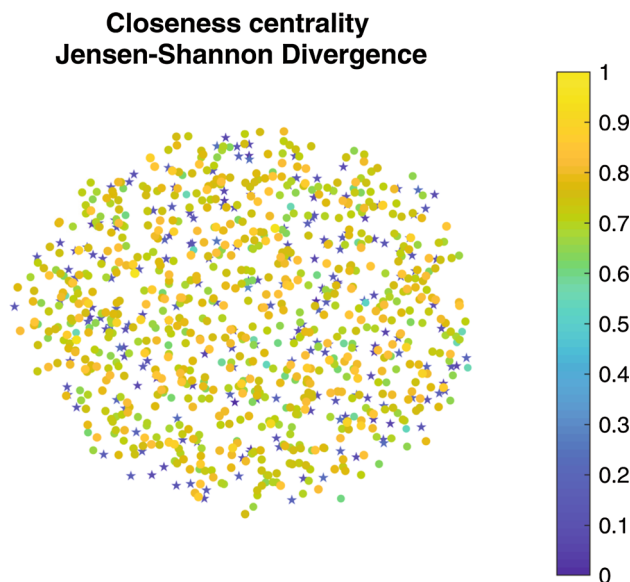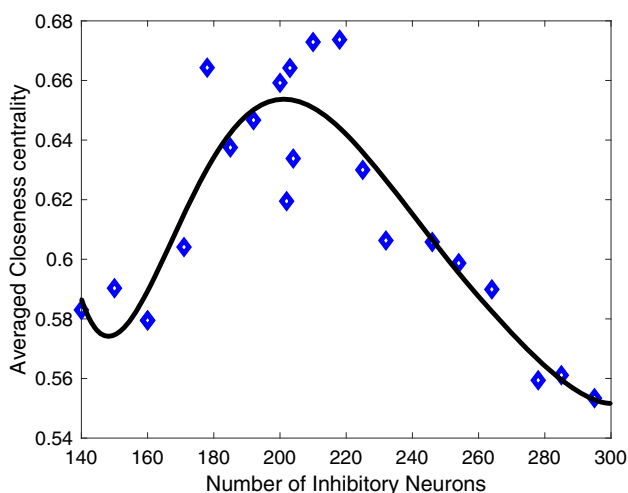
the colorbar, blue represents lower values and yellow represents higher values. We do not show the diagrams of the weighted graphs, since the edges make it difficult to appreciate the calculated measures of closeness and betweenness centrality. We estimate the closeness and betweenness centrality of the previous network considering gamma band elicited responses due to transient nociceptive circuitry dynamics. Note that Fig. 3 depicts higher values of closeness centrality for the excitatory neurons, while the inhibitory ones are close to zero. In addition, Fig. 4 depicts a betweenness centrality very close to zero independently if the neurons are excitatory or inhibitory.

To gain some insight about the behavior of the closeness centrality for the different pain configurations, in Fig. 5, we show trend of the average of this quantity for different nodes and for each configuration. The results showed in Fig. 5 suggest that there is a network configuration with a given number of inhibitory neurons close to $N_i = 200$ that might enhance information transmission when gamma activity patterns dominate the neuronal dynamics. As we change the properties of a neuron, that is, we replace an excitatory type neuron of regular spiking (RS) by a fast spiking inhibitory type (FS), the value of the closeness centrality increases reaching a maximum around $N_i = 200$ (see averaged values in Fig. 5). That is, configurations with nodes with the higher closeness score are close to $N_i = 200$ and have the shortest distances to all other nodes. When the number of inhibitory neurons is bigger than $N_i = 200$, it results in a lower average network closeness centrality and therefore represents a curtailed efficiency of the transmitted information (through a given node to all

Betweenness centrality
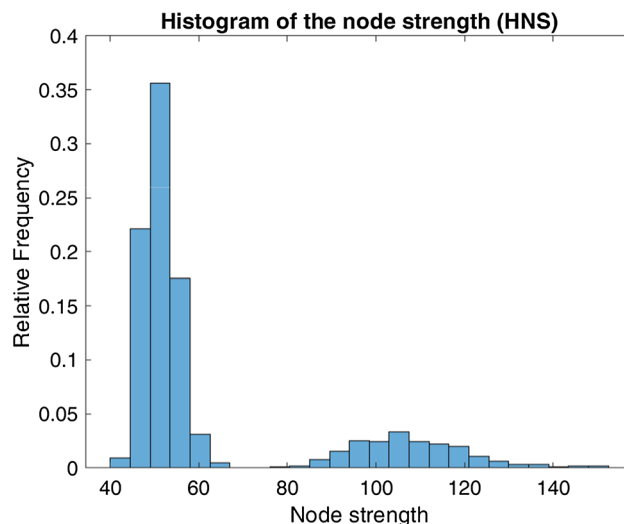## Jensen-Shannon Divergence

Fig. 4 The weighted network nodes and their betweenness centrality (normalized values). The weighted networks are constructed as in Fig. 3
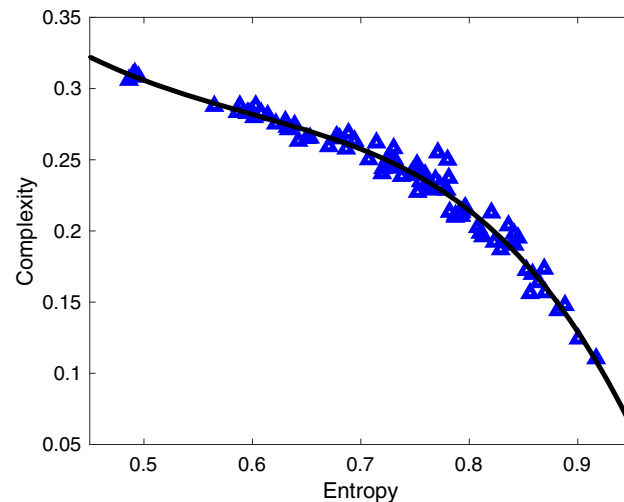

Fig. 6 Histogram of node strength (HNS). The relative frequency histogram taking 25 intervals class, $N_{\mathrm{i}} = 202$ and $N_{\mathrm{e}} = 798$

Fig. 5 Averaged closeness centrality, considering 21 different configurations of inhibitory neurons, N_{i}

Fig. 7 Causal plane $H \times C_{\mathrm{MPR}}$ considering the different configurations which presented a gamma-band elicited peak. The black line shows the fit of polynomial of degree 5

available nodes). In addition, when taking the average values of betweenness centrality, by varying the number of inhibitory neurons, they all result close to zero. This is due to the fact that several of their edges connect neurons who are already connected through others. This circuit structure behind the enhancement of the gamma band is of fundamental relevance for understanding dynamics underlying the nociceptive states.

An effective way to represent a data set is to use a bar chart to plot the frequency. In this case, the data set which we are interested in is that of node strength values. However, the number of different values is very large to use this approach (weight distribution). In these cases, you can divide the values in groups or class intervals, and then plot the number of data values

that fall at every class interval. Each class is a bin of the histogram [58]. The number of class intervals chosen must be a compensation between choosing (i) very few classes, in exchange for losing too much information on the values of the data in a class and (ii) choosing too many classes, which will result in frequencies of each class are too small for a pattern to be visible [58]. Although $5 - 10$ bins are normally used, the appropriate number of bins and of the extremes is a subjective choice and, of course, you can try different class interval numbers to see which of the resulting graphs appears to be more revealing about the data. It is common, though not essential, to choose class intervals of equal duration [58].

To gain further insights of the emergent properties of the nociceptive processing, we estimate the node
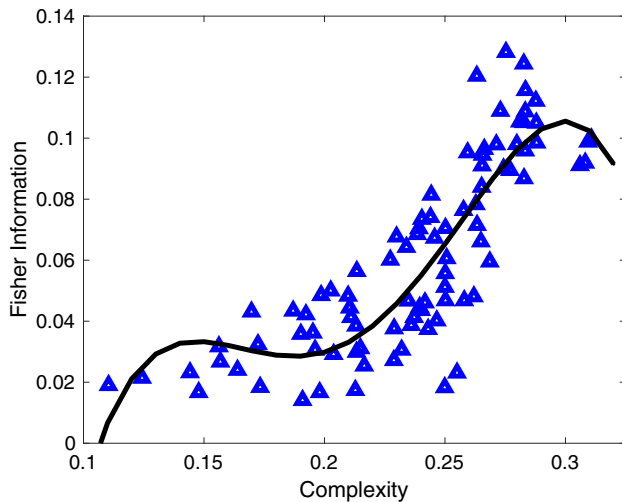
Fig. 8 Causal plane $C \times F$ taking into account all the different configurations which presented a gamma-band elicited peak as in Fig. 7. The different points correspond to dissimilar number of inhibitory neurons N_i. The black line shows the fit of polynomial of degree 5
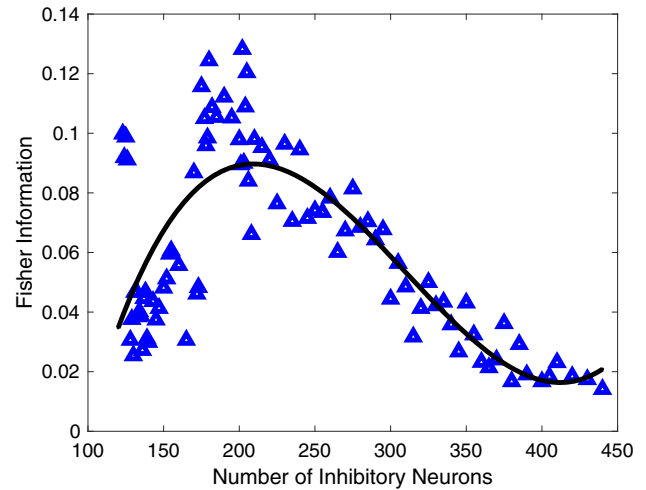
Fig. 10 Fisher information versus the number of inhibitory neurons, $N_i \times F$ considering all the configurations depicting gamma oscillations. The peak is reached when $N_i = 202$. The black line shows the fit of polynomial of degree 5
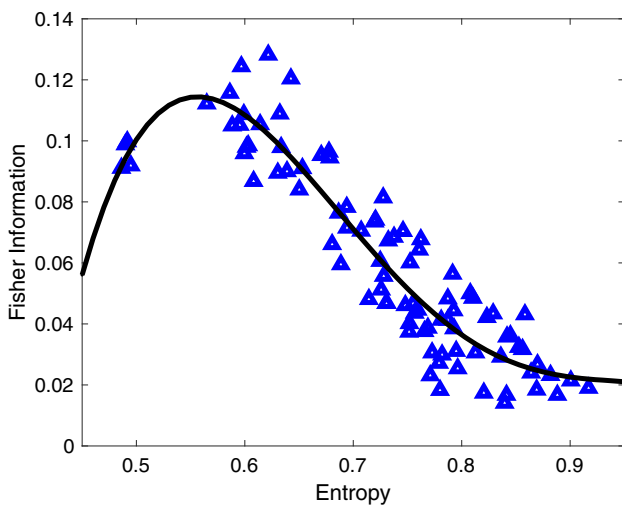
Fig. 9 Causal plane $H \times F$ taking into account all the configurations where the network exhibits gamma oscillations. The peak is reached when the number of inhibitory neurons N_i is equal to 202. The black line shows the fit of polynomial of degree 5
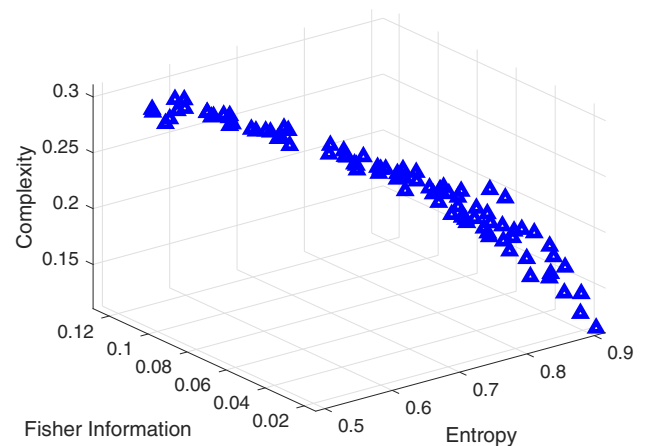
Fig. 11 Three-dimensional portrayal of the causal data quantifiers: $C_{MPR} \times F \times H$. Note the structure behind the network dynamics quantifying dissimilarities among different gamma configurations

strength as the averaged sum of weights of links connected to a given node. Figure 6 shows the relative frequency histogram of the node strength taking 25 intervals class, for the network considered in Figs. 1, 3, and 4. We decided to work with 25 class intervals. We then apply the NSB technique (see [59] for a detailed explanation of this methodology), as it ensures bias-free estimations [59,60]. Thus, we built thereafter the information planes using $H \times C_{MPR}$, $H \times F$ and $C_{MPR} \times F$, as shown in Figs. 7, 8, and 9, taking into account the different pain configurations. The curves in black being depicted in these figures are polynomial

adjustment. Figure 7 shows the causal plane $H \times C_{MPR}$, and the statistical complexity MPR decreases as Shannon entropy becomes higher for the network topologies and dynamics used previously. The degree of disorder increases as entropy increases; therefore, a system with a higher degree of entropy is characterized by a higher degree of randomness. Figure 8 depicts the causal plane $C_{MPR} \times F$, delineating a distinction between the different topologies and dynamics. In other words, Fisher's information increases non-linearly as a function of MPR statistical complexity. Figure 9 depicts the causal plane $H \times F$. Let us remark from Fig. 9 that Fisher's information reaches a maximum that occurs when the neuronal population is composed of $N = 1000$ neurons, of which $N_i = 202$ are of the inhibitory type (FS) and the remaining $N_e = 798$ are of the (RS).

Moreover, Fig. 10 depicts the behavior of Fisher information versus the number of inhibitory neurons, N_i, emphasizing that the maximum is achieved at $N_i = 202$. This network configuration, exhibiting gamma oscillations, corresponds to the number of inhibitory neurons that boost information transmission during pain-associated process, when considering a biologically plausible neuronal model. This is consistent with the idea that Fisher information peaks due to changes at both excitatory and inhibitory synapses as it function like a prime mechanism underlying neuronal circuits of pain [61–63]. Finally, Fig. 11 depicts the emerging dynamic properties of the system causal information through a three-dimensional representation: MPR statistical complexity versus Fisher information versus Shannon entropy, $C_{MPR} \times F \times H$. Notice that there is an structure defining the network dynamics quantifying dissimilarities among different network centrality graphs that characterize the gamma elicited nociceptive circuitry activity. That is, statistical complexity is maximal as entropy is in typical chaotic zone [64] and Fisher complexity increases to the highest values. Complexity decreases as entropy becomes bigger and Fisher information is curtailed, approaching non-linearly to zero.

4 Conclusion and discussion

The synchronized activity of many neurons communicating with each other generates brain wave activity [16]. Brain waves are rhythmic oscillation patterns, and in particular, the gamma-band oscillations are related to the modulation of perception and awareness that are directly linked to pain processing. In recent studies on human subjects, pain-linked gamma oscillatory activity has been reported [15,17,20,21]. However, several critical matters about what is the role of circuitry behind functional dynamics during gamma elicited pain process remain yet to be solved. Neurons in the dorsal horn process sensory information, which is then transmitted to different ensembles of neurons in the brain, including those related to pain processing [9]. The circuity in the dorsal horn is highly heterogenous making difficult to understand the mechanisms underlaying the processing of pain in the nervous system [9]. Nociceptive process can be exacerbated or decreased by means of deactivation or activation of inhibitory interneurons in the dorsal horn [7–12]. In the current work, we aim to deliver a very simple tool to gain a deeper understanding of the circuitry structure behind pain processing.

Very little is known about the neuronal circuits that process the sensory information of pain, mainly due to the heterogeneity that makes the different component of the circuits [9]. However, it is well established that the inhibitory interneurons play a crucial role on the transmission of pain as spontaneous variations in the inhibitory number of neurons can increase the pain sensations [9]. To emulate the firing activity patterns of a population of neurons, we use a biologically plausible neuronal model, where excitatory weights evolve

according to the STDP rule, capable to reproduce the prominent dynamical features of biological neurons [23,24]. From the spectral analysis of signals of the neuronal populations, it is possible to detect the presence of gamma-band oscillations patterns that are directly correlated to pain intensity [21]. We use the current model as it exhibits gamma oscillation patterns and other interesting regimes [23,24]. A similar model can be used to investigate learnable conduction delays where the high activity strongly potentiates the inhibitory synapses [65] and for spatio-temporal pattern storage [66]. Nevertheless, this would not explicitly encode the binding relations between low- and high-level features that might develop through polychronization within a hierarchical model of visual processing [67]. That is, the approach presented in this paper has broader applications, although the neuronal modeling would require some modifications depending on the subject of investigation. Gamma frequency band activity is induced in cognitive tasks and is thought to reflect underlying neural processes. Moreover, let us remark that inhibitory neurons are specially tuned to keep the gamma rhythm stable [68], and it constitutes the specific consideration guiding the current model and methodological approach to investigate pain processing.

Identifying how the network circuitry handles nociceptive information, coming from different gamma elicited oscillation patterns is of ultimate help for finding recognizable nociceptive boost in the brain and defining the dynamic framework of the modulation of pain. We study different circuitry configuration with various degree of network inter-connectivity, estimating how the closeness centrality changes when we vary the proportion of inhibitory neurons in the network, for nociceptive configurations eliciting gamma-band activity. More specifically, we use the Bandt and Pompe approach to generate probability density functions, which take into account the causality of the signal, and based on the degree of network inter-connectivity calculated through the Jensen Shannon distance, we estimate graph centrality measures. The present study allowed us to characterize the dynamics of the cortical distributions of different pain configurations, through the estimation of the closeness centrality. The averaged closeness centrality peaks when the number of inhibitory neurons is about the 20% of the total amount of neurons. That is, the averaged closeness centrality increases as the number of inhibitory neurons becomes larger reaching a peak at 20%, and for higher values of N_i, it is significantly curtailed.

To gain a deeper understanding of which configuration enhances information transmission during nociceptive process, not just based on a simple calculation of average values of the closeness centrality, we estimate the node strength distributions to investigate the Shannon entropy, the MPR complexity, and the Fisher information as the proportion of inhibitory neurons changes. Our finding shows that these types of oscillations optimize pain information transmission when the percentage of inhibitory neurons is 20% of the total number of neurons. That is, through the estimation of the informa-

tive planes $H \times C_{\text{MPR}}$, $H \times F$, and $C_{\text{MPR}} \times F$, we characterize the configurations that process information more efficiently. When the number of inhibitory neurons is $N_i = 202$ on a population of 1000 neurons, the information transmission peaks maximizing the transmission of information [61–63], and this might act as prime mechanism underlying neuronal circuits of pain. In addition, the causal plane $H \times C_{\text{MPR}}$ proves that the complexity diminishes as Shannon entropy gets higher, while the plane $C_{\text{MPR}} \times F$ shows that Fisher information raises non-linearly as complexity increases. We show that the plane $H \times F$ reaches a maximum when $N_i = 202$ neurons for a populations of 1000 neurons.

In conclusion, a network configuration with a given number of inhibitory neurons close to the 20% of the total of population improves data transmission for gamma elicited nociceptive process ruling the neuronal dynamics behind pain. Investigating the emerging dynamic properties using a three-dimensional representation $C_{\text{MPR}} \times F \times H$ allows us to determine the structure defining the network dynamics for the different gamma elicited pain circuitries. In this way, we determine which pain settings have maximum Fisher information, which means that they have a concentrated distribution, and maximum complexity, i.e., a system far from equilibrium showing a chaotic behavior [64]. This information is then conveyed efficiently, though a circuit structure with an optimal value of inhibitory neurons close to 20% of inhibitory neurons, which depicts gamma-band oscillations, can be of major significance for understanding basic elements of nociceptive states. The computer model used in this work is a highly reliable and biologically plausible model. The methodology presented in this work that combines spectral analysis techniques, with graph theory and information theory tools, is completely novel as well as the results obtained. The current work introduces a robust methodology that would be helpful for planning future experimental analysis, including indicators of deactivation or activation of inhibitory interneurons in real neurophysiological data, to characterize the dynamics of the gamma elicited topologies' configurations of pain.

Author contributions

All the authors were involved in the preparation of the manuscript. All the authors have read and approved the final manuscript.

Data Availability Statement This manuscript has no associated data or the data will not be deposited. [Authors' comment: This is a theoretical study and no experimental data has been listed.]

References

1. G. Castellani, N. Intrator, D. Remondini, Front. Genet. **5** (2014)
2. M. Rubinov, O. Sporns, Neuroimage **52**, 1059 (2010)
3. M.P. Van Den Heuvel, H.E. Hulshoff Pol, Eur. Neuropsychopharmacol. **20**, 519 (2010)
4. E.W. Lang, A. Tomé, I.R. Keck, J. Górriz-Sáez, C. Puntonet, Comput. Intell. Neurosci. **2012**, 8 (2012)
5. F. Montani, A. Oliynyk, L. Fadiga, Int. J. Neural Syst. **27**, 1650009 (2017)
6. J. Wang, X. Zuo, Y. He, Front. Syst. Neurosci. **4**, 1 (2010)
7. Ja Braz, C. Solorzano, X. Wang, A.I. Basbaum, Neuron **82**, 522 (2014)
8. A. Franois, S.A. Low, E.I. Sypek, A.J. Christensen, C. Sotoudeh, K.T. Beier, C. Ramakrishnan, K.D. Ritola, R. Sharif-Naeini, K. Deisseroth et al., Neuron **93**, 822 (2017)
9. A.J. Todd, Nat. Rev. Neurosci. **11**, 823 (2010)
10. H.C. Johannssen, F. Helmchen, J. Physiol. **588**, 3397 (2010)
11. T. Takazawa, A.B. MacDermott, Ann. N. Y. Acad. Sci. **1198**, 153 (2010)
12. W. Ren, V. Neugebauer, Mol. Pain **6**, 93 (2010)
13. F. Montani, E.B. Deleglise, O.A. Rosso, Phys. A Stat. Mech. Appl. **401**, 58 (2014)
14. R. Bardoni, K.F. Shen, H. Li, J. Jeffry, D.M. Barry, A. Comitato, Y.Q. Li, Z.F. Chen, Sci. Rep. **9**, 15804 (2019)
15. L.L. Tan, M.J. Oswald, C. Heinl, O.A.R. Romero, S.K. Kaushalya, H. Monyer, R. Kuner, Sci. Rep. **10**, 983 (2019)
16. G. Buzsaki, *Rhythms of the Brain* (Oxford University Press, Oxford, 2009)
17. M. Hauck, J. Lorenz, A.K. Engel, J. Neurosci. **27**, 9270 (2007)
18. M.N. Baliki, A.T. Baria, A.V. Apkarian, J. Neurosci. **31**, 13981 (2011)
19. M. Ploner, C. Sorg, J. Gross, Trends Cogn. Sci. **21**, 100 (2017)
20. J. Gross, A. Schnitzler, L. Timmermann, M. Ploner, PLoS Biol. **5**, e133 (2007)
21. Z. Zhang, L. Hu, Y. Hung, A. Mouraux, G. Iannetti, J. Neurosci. **32**, 7429 (2012)
22. E.S. May, M.M. Nickel, S.T. Dinh, L. Tiemann, H. Heitmann, I. Voth, T.R. Tölle, J. Gross, M. Ploner, Hum. Brain Mapp. **40**, 293 (2019)
23. E.M. Izhikevich, IEEE Trans. Neural Netw. **14**, 1569 (2003)
24. E.M. Izhikevich, Neural Comput. **18**, 245 (2006)
25. R. Baravalle, N. Guisande, M. Granado, O.A. Rosso, F. Montani, Front. Phys. **7**, 115 (2019)
26. O. Rosso, C. Masoller, Phys. Rev. E **79**, 040106(R) (2009)
27. O. Rosso, C. Masoller, Eur. Phys. J. B **69**, 37 (2009)
28. O. Rosso, F. Olivares, A. Plastino, Paper Phys. **7**, 070006 (2015)
29. F. Montani, O.A. Rosso, Entropy **16**, 4677 (2014)
30. E.M. Izhikevich, *Dynamical Systems in Neuroscience* (MIT Press, Cambridge, 2007)
31. L. Risinger, K. Kaikhah, *Innovations in Applied Artificial Intelligence* (Springer, Berlin, 2004), pp. 1033–1042

32. T. Schwalger, L. Schimansky-Geier, Phys. Rev. E Stat. Nonlinear Soft Matter Phys. **77**, 031914 (2008)
33. K.S. Kravtsov, M.P. Fok, P.R. Prucnal, D. Rosenbluth, Opt. Express **19**, 2133 (2011)
34. C. Bandt, B. Pompe, Phys. Rev. Lett. **88**, 174102 (2002)
35. F. Olivares, A. Plastino, O. Rosso, Phys. A **391**, 2518 (2012)
36. F. Olivares, A. Plastino, O. Rosso, Phys. Lett. A **376**, 1577 (2012)
37. F. Montani, O.A. Rosso, F.S. Matias, S.L. Bressler, C.R. Mirasso, Philos. Trans. R. Soc. Lond. Ser. A **373**, 20150110 (2015)
38. F. Montani, R. Baravalle, L. Montangie, O.A. Rosso, Philos. Trans. R. Soc. Lond. Ser. A **373**, 20150109 (2015)
39. C. Shannon, W. Weaver, *The Mathematical Theory of Communication* (University of Illinois Press, Champaign, 1949)
40. T.M. Cover, J.A. Thomas, *Elements of Information Theory* (Wiley-Interscience, New York, 2012)
41. B. Frieden, *Science from Fisher Information: A Unification* (Cambridge University Press, Cambridge, 2004)
42. R. Lopez-Ruiz, H.L. Mancini, X. Calbet, Phys. Lett. A **209**, 321 (1995)
43. C. Tsallis, *Introduction to Nonextensive Statistical Mechanics* (Springer, Berlin, 2009)
44. A. Renyi, *On measures of entropy and information*, in *Fourth Berkeley Symposium on Mathematical Statistics and Probability*, pp. 547–561 (1961)
45. W.K. Wootters, Phys. Rev. D **23**, 357 (1981)
46. S. Kullback, R.A. Leibler, Ann. Math. Stat. **22**, 79–86 (1951)
47. I. Grosse, P. Bernaola-Galván, P. Carpena, R. Román-Roldán, J. Oliver, H.E. Stanley, Phys. Rev. E Stat. Nonlinear Soft Matter Phys. **65**, 041905 (2002)
48. F. Montani, O.A. Rosso, S.R. Schultz, AIP Conf. Proc. **913**, 184 (2007)
49. M. Martín, A. Plastino, O. Rosso, Phys. A **369**, 439 (2006)
50. O. Rosso, H. Larrondo, M. Martín, A. Plastino, M. Fuentes, Phys. Rev. Lett. **99**, 154102 (2007)
51. L.C. Freeman, Soc. Netw. **1**, 215 (1979)
52. L.C. Freeman, D. Roeder, R.R. Mulholland, Soc. Netw. **2**, 119 (1979/1980)
53. D.S. Bassett, E.T. Bullmore, Curr. Opin. Neurol. **22**, 340 (2009)
54. E.T. Bullmore, O. Sporns, Nat. Rev. Neurosci. **10**, 186 (2009)
55. C.J. Stam, J.C. Reijneveld, Nonlinear Biomed. Phys. **1**, 3 (2007)
56. M. Newman, *Networks: An Introduction* (Oxford University Press, Oxford, 2010)
57. E. Brigham, R. Morrow, Spectr. IEEE **4**, 63 (1967)
58. S. Ross, *Introduction to Probability Models* (Academic Press, New York, 2009)
59. R. Baravalle, O. Rosso, F. Montani, Chaos Interdiscip. J. Nonlinear Sci. **28**, 075513 (2018)
60. I. Nemenman, W. Bialek, RdR van Stevenink, Phys. Rev. E **69**, 056111 (2004)
61. M. Prokopenko, J.T. Lizier, O. Obst, X.R. Wang, Phys. Rev. E Stat. Nonlinear Soft Matter Phys. **84**, 041116 (2011)
62. M. Prokopenko, J.T. Lizier, Sci. Rep. **4** (2014)
63. M. Prokopenko, L. Barnett, M. Harr, J.T. Lizier, O. Obst, X.R. Wang, Proc. R. Soc. A **471**, 20150610 (2015)
64. O. Rosso, F. Olivares, L. Zunino, L. De Micco, A. Aquino, A. Plastino, H. Larrondo, Eur. Phys. J. B **86** (2012)
65. H. Paugam-Moisya, R. Martineza, S. Bengio, Nat. Rev. Neurosci. **71**, 1143 (2008)
66. R. Wang, G. Cohen, K. Stiefel, T. Hamilton, J. Tapson, A. van Schaik, Front. Neurosci. **7**, 14 (2013)
67. A. Eguchi, J.B. Isbister, N. Ahmad, S. Stringer, Psychol. Rev. **125**, 545 (2018)
68. M.N. Economo, J.A. White, PLoS Comput. Biol. **8**, e1002354 (2018)